Applied Catalysis B: Environmental 224 (2018) 705–714

Contents lists available at ScienceDirect

Applied Catalysis B: Environmental

journal homepage: www.elsevier.com/locate/apcatb

Research paper

Black NiO-TiO_2 nanorods for solar photocatalysis: Recognition of electronic structure and reaction mechanism

Jie Liu[a], Ying Li[a], Jun Ke[b], Shaobin Wang[c,*], Lidong Wang[a], Huining Xiao[a,*]

[a] Department of Environmental Science & Engineering, North China Electric Power University, Baoding 071003, China
[b] School of Chemistry and Environmental Engineering, Wuhan Institute of Technology, Wuhan 430073, China
[c] Department of Chemical Engineering, Curtin University, GPO Box U1987, Perth, WA 6845, Australia

ARTICLE INFO

Keywords:
Photocatalysis
Black NiO nanoclusters
TiO_2 nanorods
p-n heterojunctions
Toluene degradation

ABSTRACT

This work provides an engineering guide to construct active sites on TiO_2 nanorods (NRs) by coupling *p*-type black NiO nanoclusters (E_g = 1.42 eV) with rich crystal defects and match-up band structure for excellent solar photocatalysis. Photo-oxidation of toluene was used as a model reaction to evaluate the photocatalytic performance of black NiO/TiO_2 hybrids under simulated solar light irradiation from a 300 W Xe-lamp. The black NiO/TiO_2 hybrids Exhibit 80% of photodegradation conversion and 56% of mineralization efficiency, which are 7.9 and 4.5 times higher than those of TiO_2 NRs. Detailed characterizations reveal that highly dispersed NiO and *p-n* heterojunction effectively facilitate light-harvesting, separation and transfer of photo-generated charge carriers, and significantly inhibit the recombination of electrons and holes. Furthermore, the realignment of band structure and the *p-n* heterojunctions in NiO/TiO_2 result in the production of $\cdot O_2^-$ and h^+ with a longer lifetime, which could efficiently attack the aromatic ring of toluene. The efficient adsorption of toluene by H-bonding formation also facilitates the photo-oxidation of toluene on NiO/TiO_2.

1. Introduction

From the sustainable point of view, sunlight-driven photocatalysis for environmental remediation and water splitting to hydrogen are promising approaches to solve the increasing environmental issues and energy crisis [1–4]. Heterogeneous photocatalysis employs a solid photocatalyst to adsorb solar light in producing electron-hole pairs for chemical reactions. Subsequently, the target substances are oxidized or reduced by the generated holes or electrons, respectively, to form desirable chain reactions to products. The key issue of this process is development of novel photocatalysts with high photocatalytic performance [5–7].

An excellent photocatalyst for photocatalytic environmental remediation should be not only efficient to utilize sunlight but also nontoxic and earth-abundant. Over the past 40 years, TiO_2 has been the most studied material in photocatalysis, owing to its suitable energetic positions of band edges and high photocatalytic activity, as well as low cost, good stability and nontoxicity. Nevertheless, a wide band gap (E_g = ~3.2 eV for anatase) and rapid recombination of photogenerated electron-hole pairs are major drawbacks inhibiting its further application [8–12]. Numerous efforts have been carried out to prepare tailored TiO_2 materials, such as doping, dye sensitization, and surface modification. Fabrication of semiconductor heterojunction by coupling TiO_2 with narrow band gap substances has also been explored as an efficient strategy, which could enhance solar light response, improve the separation of photoinduced electrons and holes, and inhibit their recombination [13–15].

Among various transition metal oxides, NiO has been extensively investigated due to its interesting 3d electronic structure, which are localized in space but spread out over a wide energy range because of strong coulomb repulsion between them [16,17]. This unique electronic distribution leads to high mobility of charge carriers in NiO, making it as a cocatalyst in the photocatalytic water splitting, dye sensitized solar cells and thin film photovoltaics [13,18–20]. Moreover, NiO is a typical *p*-type semiconductor, and the *p-n* heterojunctions at the interface between NiO and TiO_2 favors the further inhibition of the recombination of photo-generated electrons and holes [21,22]. Nevertheless, NiO is generally reported as a wide band-gap semiconductor with E_g = ~3.5 eV, precluding it from absorbing visible light, and as a suitable candidate for surface modification of TiO_2 [23,24]. On the other hand, a novel black TiO_2 with a wealth of defects has been recently reported, displaying an excellent visible light response. Therefore, it is possible to optimize the optical property of semiconductors by darkening the color, which could be accomplished by the introduction of

* Corresponding authors.
E-mail addresses: shaobin.wang@curtin.edu.au (S. Wang), huiningxiao@hotmail.com (H. Xiao).

https://doi.org/10.1016/j.apcatb.2017.11.028
Received 12 September 2017; Received in revised form 7 November 2017; Accepted 11 November 2017
Available online 11 November 2017

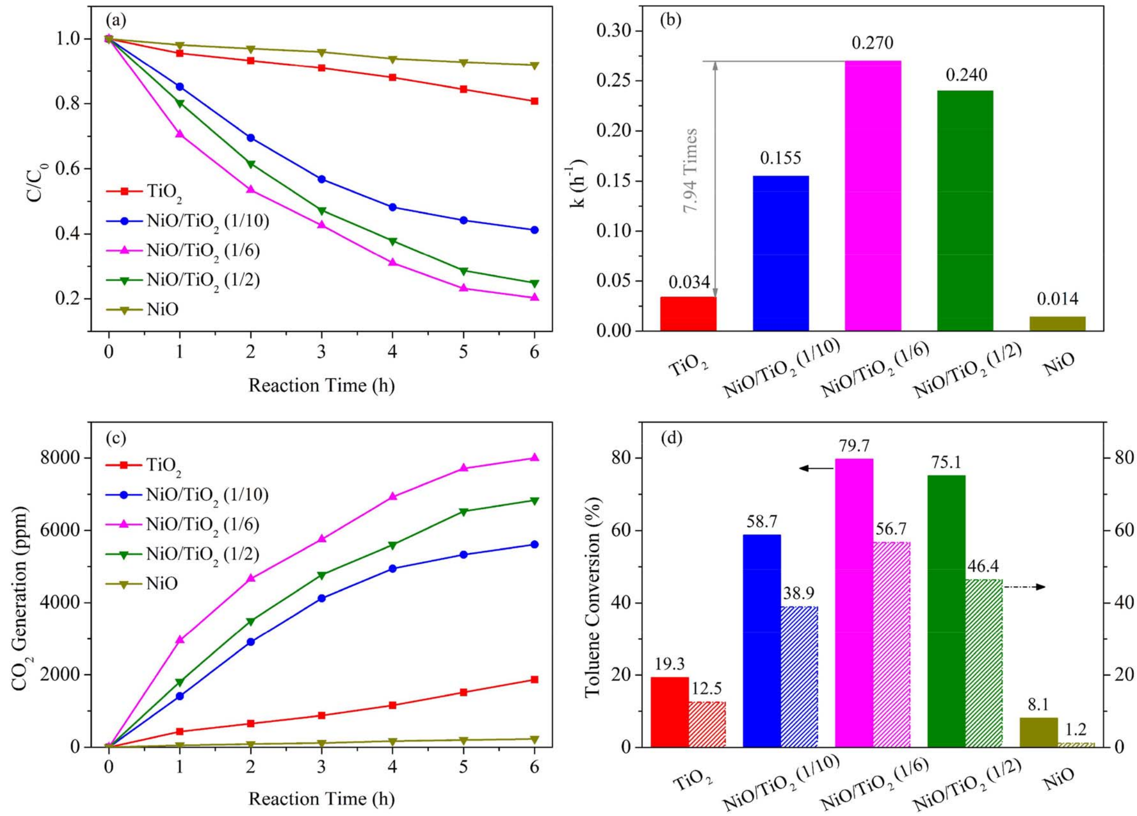

Fig. 1. (a) Performance of the various catalysts in the photo-oxidation of toluene under Xe-lamp irradiation, (b) the pseudo-first-order kinetic constants, (c) CO_2 generation, and (d) the corresponding toluene conversion and the mineralization efficiency.

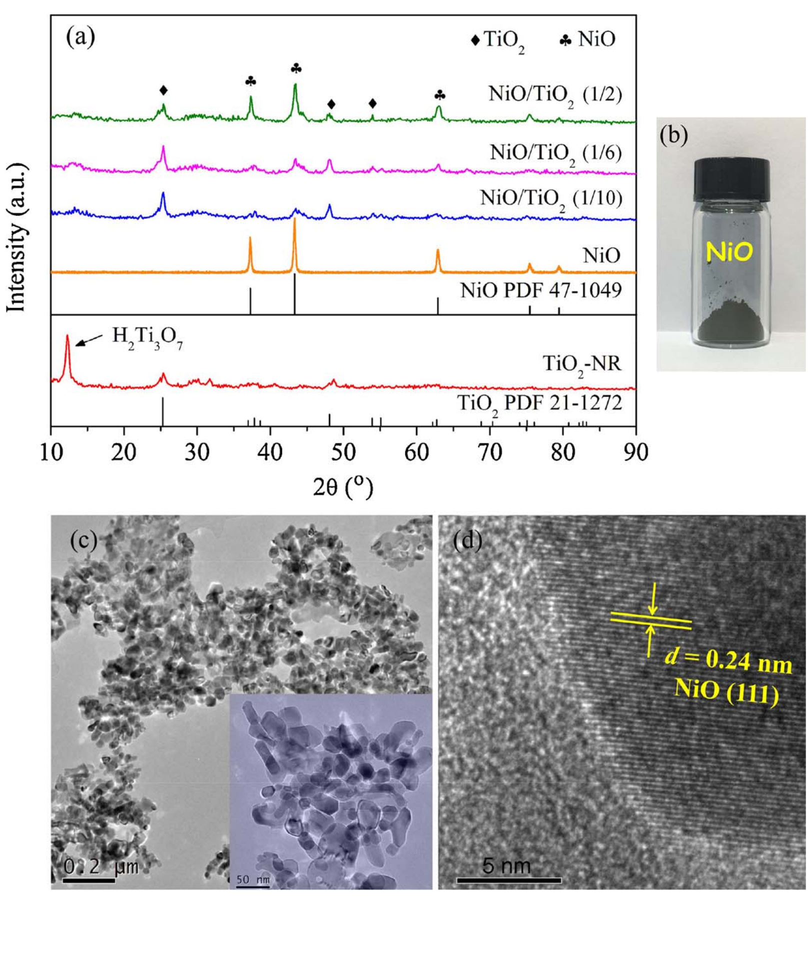

Fig. 2. (a) XRD patterns of as-prepared TiO_2 NRs, NiO and various NiO/TiO_2 photocatalysts, (b) Photograph of the as-prepared black NiO, (c) TEM images of NiO nanoparticles, the inset: enlarged TEM image of NiO nanoparticles, and (d) HRTEM images of NiO nanoparticles.

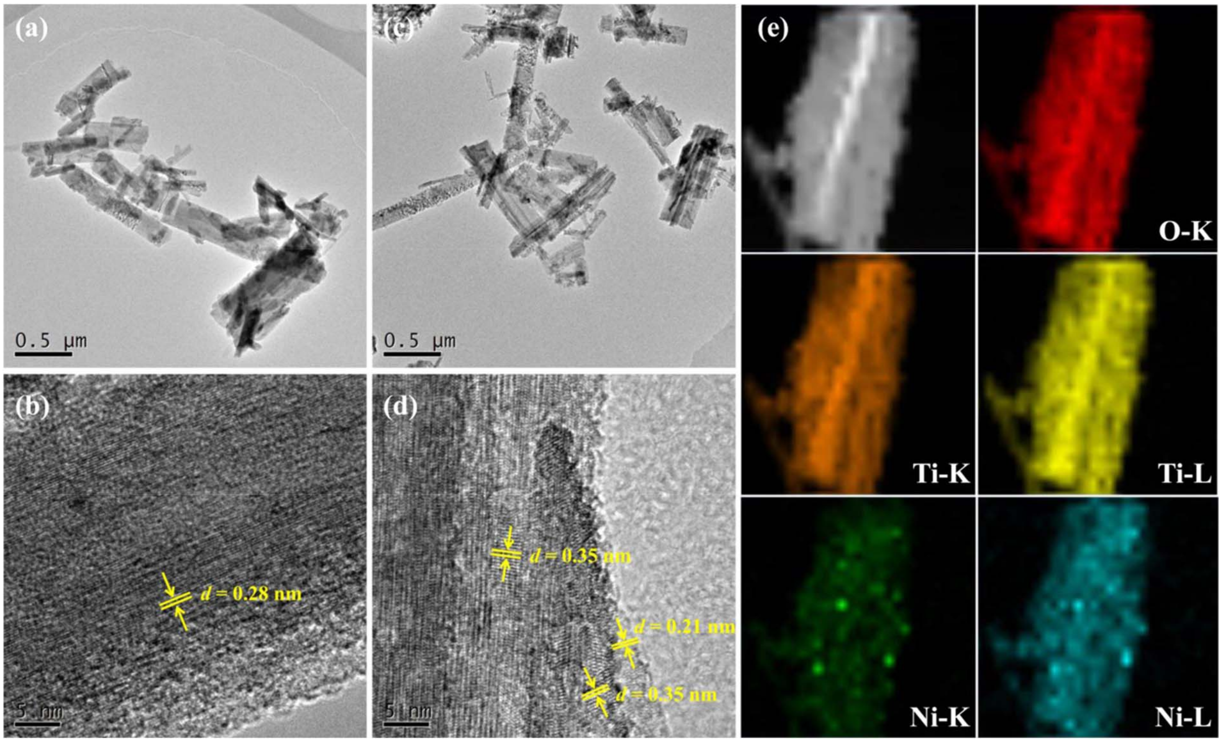

Fig. 3. TEM images of TiO_2 NRs (a) and NiO/TiO_2 (1/6) (c) samples, HRTEM images of TiO_2 NRs (b) and $NiO/TiO_2(1/6)$ (d) samples, and the element mapping of a selected nanorod of $NiO/TiO_2(1/6)$ (e).

atomic defects through the controlling of synthesis conditions or the reductive post-treatment process [10,25–27]. However, no attempt has been made for black NiO with TiO_2 for photocatalysis.

In this work, we present a study on synthesis of a novel dark NiO nanoparticle (black NiO nanoclusters) with a significantly narrowed band gap of ~1.42 eV. Atom defects and intermediate energy level were introduced into the black NiO, while the black NiO still maintains its *p*-type characteristic. It is demonstrated that the surface modification of TiO_2 nanorods by the black NiO nanoclusters enlarges the light response range and simultaneously inhibits recombination of photo-generated electrons and holes, attributed to the realignment of band structure and formation of *p-n* heterojunction in NiO/TiO_2 hybrids. The photocatalytic activity and degradation mechanism was evaluated by the photo-oxidation of gaseous toluene, monitored by *in situ* FTIR in detail. This work provides important development in new black semiconductors with a wide light-absorption region, as an effective way for the rational design of TiO_2-based hybrid photocatalysts, as well as for insights into catalyst structure and reaction mechanism.

2. Experimental

2.1. Synthesis of photocatalysts

The black NiO nanoparticles were prepared by a facile hydrothermal method. Nickel nitrate ($Ni(NO_3)_2{\cdot}6H_2O$) at 5 mmol and urea at 15 mmol were dissolved in a mixture of deionized (DI) water and ethanol with a volume ratio of 2/1 (75 mL), and ultrasonically treated for 30 min. The solution was transferred into a 100 mL Teflon-lined autoclave and maintained at 120 °C for 12 h. The obtained slurry was washed by DI water and ethanol, dried at 60 °C for 12 h, and calcined at 500 °C for 2 h in air.

For preparation of TiO_2 nanorods (TiO_2 NRs), commercial P25 (0.2 g) was immersed in 40 mL of 10 M NaOH solution. The suspension was transferred to a 50 mL Teflon-lined autoclave and maintained at 180 °C for 24 h. The obtained slurry was washed by 0.1 M HCl solution until the pH value decreased to ~2, followed by washing with DI water and ethanol. Then the sample was dried at 60 °C for 12 h, and annealed at 500 °C in air for 4 h to obtain TiO_2 NRs.

In a typical preparation of black NiO/TiO_2 hybrid photocatalysts, 2 mmol of TiO_2 NRs, a certain amount of $Ni(NO_3)_2{\cdot}6H_2O$ and 15 mmol urea were immersed in the mixture of DI water and ethanol with a volume ratio of 2/1 (75 mL) for ultrasonication of 30 min. The suspension was then transferred to a Teflon-lined autoclave (100 mL) and maintained at 120 °C for 12 h. The obtained slurry was washed by DI water and ethanol, dried at 60 °C for 12 h, and calcined at 500 °C for 2 h in air to obtain black NiO/TiO_2 hybrid photocatalysts. The products were denoted as $NiO/TiO_2(1/x)$, where x is the molar ratio of TiO_2/NiO in the synthesis.

2.2. Characterizations

The morphology of the as-prepared materials was observed by a field-emission scanning electron microscope (FE-SEM, Neon40esb Zeiss), transmission electron microscope (TEM, FEI-Tecnai G^2 F20 S-TWIN) and high-resolution transmission electron microscope (HR-TEM, FEI-Tecnai G^2 F20 S-TWIN). X-ray diffraction (XRD) was carried out on a Bruker D8-Advanced X-ray instrument using Cu Kα radiation (λ = 1.5418 Å). X-ray photoelectron spectroscopy (XPS) and valence band XPS (VB-XPS) of various samples were carried out on a Kratos AXIS Ultra DLD system under ultrahigh vacuum (UHV) conditions with a base pressure less than 1×10^{-9} mb, and the binding energies of C 1s, Ni 2p, Ti 3d and O 1 s were calibrated using C 1s (BE = 284.8 eV) as a standard. UV–vis diffuse reflection spectroscopy (DRS) was carried out on an UV–vis spectrophotometer (JASCOV-670) with a wavelength range of 200–800 nm. The formation of $\cdot OH$ and $\cdot O_2^-$ radicals under light illumination was confirmed by the Electron Spin Resonance (EPR) spectra, recorded by using 5, 5-dimethyl-1-pyrroline (DMPO, > 99.0%) as a probe on a Bruker EMS-plus instrument, operated under the following conditions: center field of 3520 G, sweep width of 100 G, microwave frequency of 9.87 GHz, power setting of 18.75 mW, and the scan number of 3.

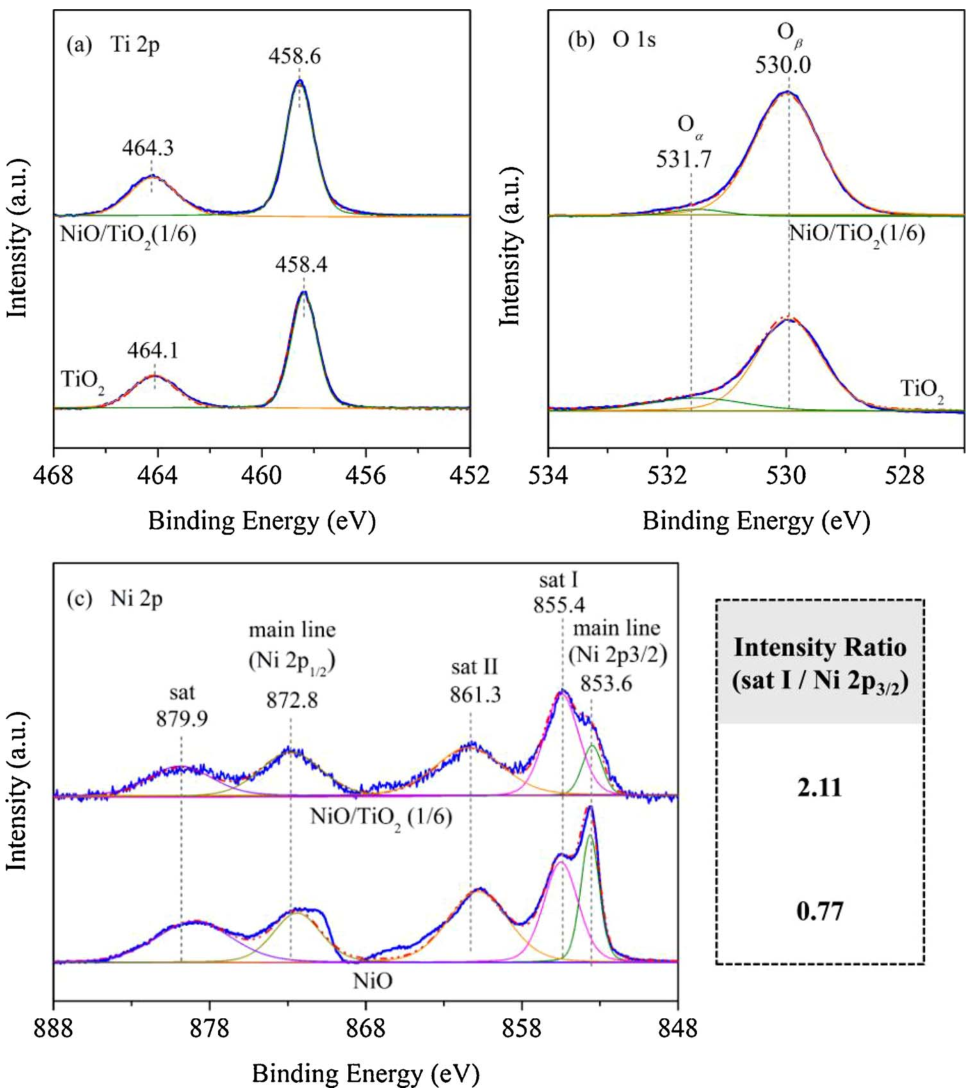

Fig. 4. XPS spectra of Ti 2p (a), O 1s (b) and Ni 2p (c) of the as-prepared photocatalysts.

2.3. Photoelectrochemical (PEC) tests

The PEC measurements were carried out using a Chi 660e electrochemical workstation operated in a standard three-electrode cell with a fluorine-doped tin oxide (FTO) electrode deposited with the as-prepared catalyst as a photoanode, a saturated calomel electrode (SCE) as the reference electrode and a Pt wire as the counter electrode. For the fabrication of the working electrode, 40 mg catalyst was mixed with a certain amount of ethanol and Nafion solution homogeneously, and the obtained sample was deposited in a thin film on the FTO glass with a controlled area of 1 cm^2 using spin-coating, and then dried at 60 °C for 30 min to form a film electrode. The PEC performance of the catalysts was measured under a 300 W Xe-lamp, and 0.5 M Na_2SO_4 solution (40 mL, pH = 6.8, 25 °C). The electrochemical impedance spectroscopy (EIS) was carried out in the frequency range of $10^{-1} \sim 10^5$ Hz. The electrode potential versus saturated calomel electrode (SCE) can be converted to reversible hydrogen electrode (RHE) potential by the Nernst equation as follows:

$$V_{NHE} = V_{SCE} + V^0{}_{SCE} \tag{1}$$

where V_{NHE} is the converted potential *vs* NHE, $V^0{}_{SCE} = 0.245$ V at pH = 6.8, 25 °C, and V_{SCE} is the experimental potential measured against a Hg/Hg_2Cl_2/saturated KCl reference electrode.

2.4. Photocatalytic activity evaluation

The photocatalytic activity of the as-prepared samples was evaluated by the photocatalytic degradation of aqueous methylene blue (MB) and gaseous toluene, which were widely used as typical organic dye pollutants in wastewater and volatile organic compounds (VOCs) in indoor air, respectively. The reactions were carried out under the irradiation of a solar simulator, 300 W Xe-lamp (CEL-PE300L-3A, 500 mW/cm^2). For the degradation of MB solution (20 ppm), the photocatalyst (200 mg L^{-1}) was first immersed in the MB solution in dark for 30 min to establish adsorption-desorption equilibrium prior to illumination. The concentration of MB at different reaction time was analyzed at its characteristic absorption wavelength of 664 nm on a UV–vis spectrophotometer (JASCOV-670). Meanwhile, the mineralization efficiency of the reaction was investigated by total organic carbon (TOC) measurement (Analytik jena, muli N/C 3100).

The photo-oxidation of gaseous toluene was carried out in a homemade quartz reaction cell containing a catalyst of 20 mg, gas-phase toluene of ~3000 ppm in air, with the relative humidity of 40% at reaction temperature of ~25 °C. The concentrations of toluene and the generated CO_2 at varying irradiation time were measured by a gas chromatography (GC, Agilent 7890 II), and the mineralization efficiency of toluene on various catalysts was calculated by the followed equation:

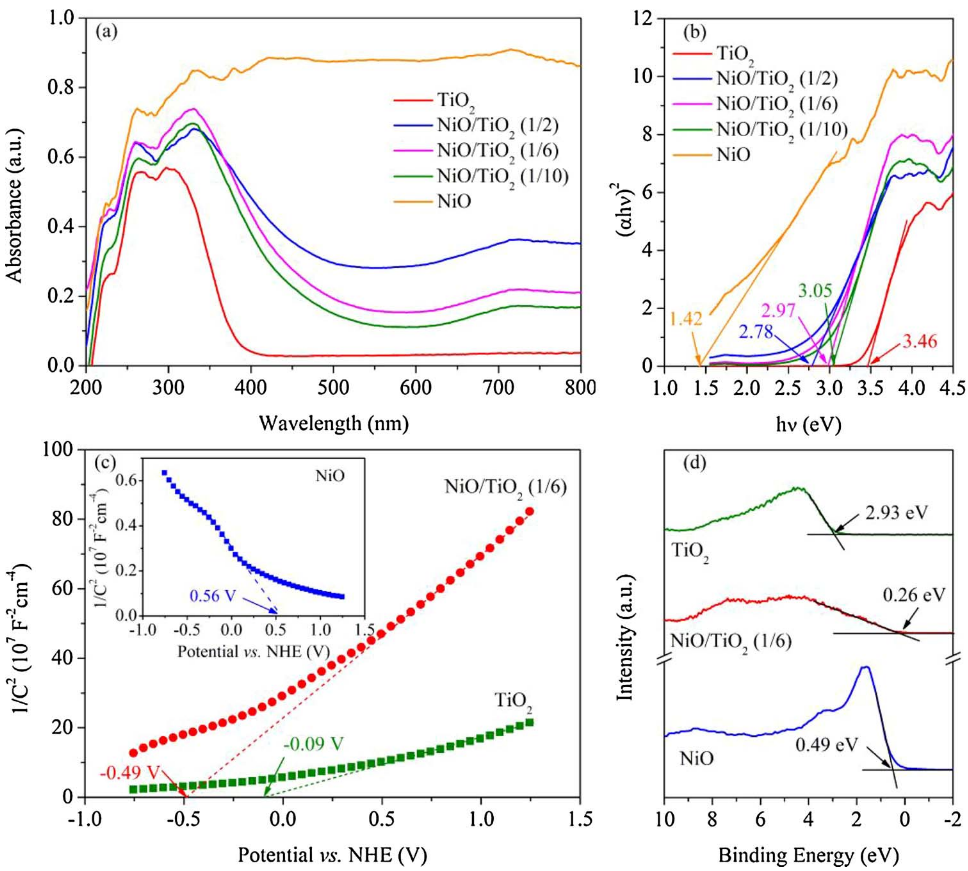

Fig. 5. (a) DRS of TiO_2, NiO and various NiO/TiO_2 and (b) their corresponding plots of $(\alpha h\nu)^2$ *vs.* photon energy, (c) Mott-Schottky plots for TiO_2, NiO and NiO/TiO_2(1/6) electrodes, (d) valance band XPS spectra of TiO_2, NiO and NiO/TiO_2(1/6) electrodes.

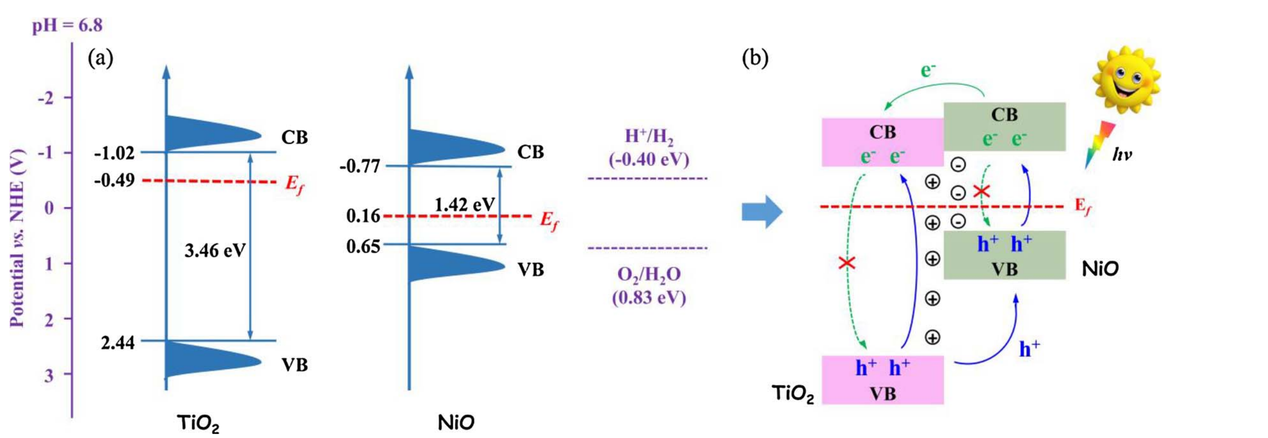

Fig. 6. (a) Band positions of TiO_2 NRs and black NiO according to the band gaps, flat band potentials, and VB positions obtained from Fig. 5, (b) approximate band position of NiO/TiO_2(1/6) catalyst and the proposed mechanism for the enhanced charge transfer on the catalyst.

$$\text{Mineralizaiton efficiency} = \frac{C_C}{7C_0} \times 100\%$$

where C_0 and C_C are the concentrations of the initial gas phase toluene and the generated CO_2 at time t, expressed by ppm. The amount of theoretically generated CO_2 is represented by $7C_0$ *based on a complete oxidation*.

The stability of the as-prepared catalysts was also carried out. For the photo-degradation of MB solution, the catalyst was recycled by washing with ethanol and drying, and then used for the test of catalyst stability. For the photo-oxidation of toluene, the catalyst was recycled after calcination at 500 °C for 2 h in air.

2.5. In-situ fourier transform infrared spectroscopy (FTIR)

The surface adsorbed species as well as their transformation during the photo-oxidation of toluene was further investigated by *in situ* FTIR (Bruker Sennor II). All spectra were recorded over accumulative 32 scans with a resolution of 4 cm^{-1} in a range of 4000–400 cm^{-1}.

3. Results and discussion

3.1. Photocatalytic activity tests

The photocatalytic activities of P25, as-prepared TiO_2 NRs, black NiO and various NiO/TiO_2 catalysts were firstly evaluated by photo-degradation of MB solution. As presented in Fig. S1a (Supporting

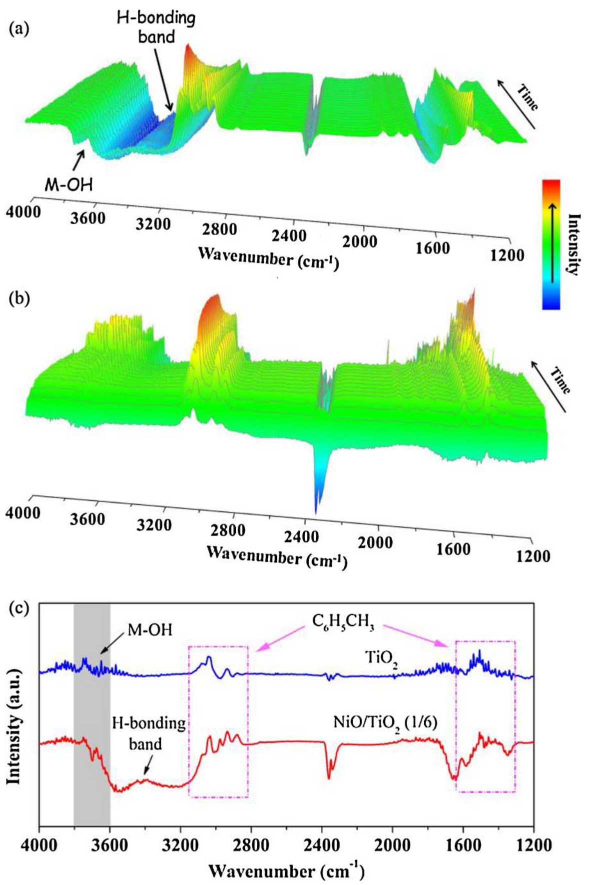

Fig. 7. *In situ* FTIR spectra on $NiO/TiO_2(1/6)$ (a) and TiO_2 (b) samples during the toluene adsorption, and (c) FTIR spectra of $NiO/TiO_2(1/6)$ and TiO_2 after toluene saturation.

Information), the commercial P25 exhibits a weak activity for the photo-degradation of MB, while the removal of MB on the re-constructed TiO_2 NRs is significantly promoted, though mainly attributing to its excellent adsorption. For black NiO and NiO/TiO_2 samples, NiO/TiO_2 samples exhibit the similar performance, which are improved significantly compared with that of the black NiO, and the most appropriate molar ratio for the coupling of NiO and TiO_2 is at 1/6. The reaction selectivity of the photo-degradation of MB is reflected by the TOC concentration in products as presented in Fig. S1b (Supporting Information), and the TOC concentration of ~10% suggests the similar mineralization efficiency of various catalysts. Zeta potentials of various samples were also measured (Table S1 in Supporting Information). The as-prepared TiO_2 and NiO/TiO_2 hybrids exhibit the opposite charge to MB solution, which favors the surface adsorption of MB and the further degradation, while the adsorption of NiO to MB is quite weak due to the surface charge repulsion. The activity of the precursor for TiO_2 NRs is also tested, which is confirmed as $H_2Ti_3O_7$ and exists with anatase TiO_2 in TiO_2 NRs from the XRD pattern as below (Fig. 2a). The precursor exhibits a higher activity than P25 and a slightly weaker performance than the as-prepared TiO_2 NRs, herein, it is speculated that the $H_2Ti_3O_7$ phase would exhibit neither a significant promotion nor inhibition effect for the activity of TiO_2 NRs.

Based on the MB photo-degradation, TiO_2 NRs, NiO and various NiO/TiO_2 composites were further applied in the photo-oxidation of toluene with a concentration of 3000 ppm, to investigate the promoting effect of NiO on the photocatalytic activity. From Fig. 1a, it is obvious that the NiO/TiO_2 hybrids exhibit much elevated activity for the photo-oxidation of toluene compared with TiO_2 NRs, and that the removal efficiency of toluene over TiO_2 NRs, $NiO/TiO_2(1/10)$, $NiO/TiO_2(1/6)$, $NiO/TiO_2(1/2)$ and NiO samples achieve 19, 59, 80, 75 and 8.1%, respectively, after irradiation for 6 h. The reaction rate is represented by the apparent rate constants (k) from the degradation curves of $-\ln(C/C_0)$ *vs* irradiation time, illustrating that the photocatalytic rates of $NiO/TiO_2(1/6)$ is elevated to 7.94 times of that of TiO_2 (Fig. 1b). The concentrations of generated CO_2 and the mineralization efficiency of toluene on various catalysts are presented in Fig. 1c and d, from which the as-prepared $NiO/TiO_2(1/6)$ exhibits a good reaction selectivity toward CO_2. The activity of $NiO/TiO_2(1/6)$ sample for photo-oxidation of toluene is also compared with some catalysts reported previously, including commercial TiO_2, various modified TiO_2 and Bi_2WO_6 materials [28–32]. The results are summarized in Table S2 (Supporting Information), and suggest the excellent activity of the as-prepared catalyst.

Additionally, the recycling tests of $NiO/TiO_2(1/6)$ for both of the photo-degradations of MB and toluene were also carried out, and the results (Fig. S2, Supporting Information) suggest its good stability. From Fig. 1 and Fig. S1 and S2, the black NiO exhibit a significant sensitization for TiO_2 to improve the TiO_2 photocatalytic activity, and the satisfactory photocatalytic performances of $NiO/TiO_2(1/6)$ in the photo-degradations of MB solution and gaseous toluene also suggests its possible broadened application compared with TiO_2.

3.2. Characterizations

3.2.1. Structure and morphology

The phase and crystal structure of the as-prepared TiO_2 NRs, NiO and various NiO/TiO_2 photocatalysts were investigated by XRD (Fig. 2a). The XRD pattern of the as-prepared TiO_2 NRs suggests a mixed phase of $H_2Ti_3O_7$ and anatase TiO_2, and the presence of the $H_2Ti_3O_7$ at 11.2° could be due to the uncomplete calcination of the precursor (PDF#47-0561). The other two diffraction peaks centered at 25.4° and 48.1° are assigned to the (101) and (200) planes of anatase TiO_2, respectively (PDF#21-1272). The XRD pattern of the as-prepared NiO is quite identical to that of bunserite NiO (PDF#47-1049), in which the peaks centered at 37.3°, 43.3° and 62.9° are attributed to the (111), (200) and (220) planes of NiO, respectively. For the NiO/TiO_2 samples, the diffraction peaks ascribed to NiO are detected, and the transformation of $H_2Ti_3O_7$ to TiO_2 makes it possible to form a NiO/TiO_2 heterojunctions with strong interaction. The black color of the as-prepared NiO is shown in Fig. 2b, which could be attributed to the lattice defects and its nanoscale size [13]. The diameter of the black NiO nanoparticles are ~20 nm (Fig. 2c), and the lattice defects are demonstrated by its ambiguous lattice structure as seen in the HRTEM image (Fig. 2d), though the characteristic distance of the (111) plane of NiO can be observed distantly. From the reference [13], the black color and the lattice defects of the as-prepared NiO suggest the excellent light response and the possibly improved carrier collection. Due to the different loadings of NiO and diverse strength to TiO_2 support, the colors of the NiO/TiO_2 (1/10), (1/6) and (1/2) samples change from yellow to light grey and further to dark grey (Fig. S2, Supporting Information).

The morphology of the synthesized TiO_2 NRs was investigated by TEM (Fig. 3a), confirming its regular nanorod structure with an average diameter of ~180 nm. The lattice spacing of 0.28 nm is ascribed to the (311) plane of $H_2Ti_3O_7$ (Fig. 3b), without the anatase TiO_2 due to its low crystallization, which is good in agreement with the XRD results. $NiO/TiO_2(1/6)$ sample maintains the uniform morphology of nanorods (Fig. 3c). Fig. 3d displays the HRTEM and SAED images of $NiO/TiO_2(1/6)$, in which the interplane distance of 0.35 nm matches well with the (101) plane of anatase TiO_2, and the d spacing of 0.21 nm is assigned to the (200) plane of NiO. From the HRTEM of NiO/TiO_2 (1/6), the loaded NiO nanoparticles are considered to attach on the surface of TiO_2, and the proximity of the (200) plane to the (111) plane implies the possible formation of heterojunction between NiO and TiO_2. The elemental mapping of a selected $NiO/TiO_2(1/6)$ nanorod is presented in Fig. 3e, and the homogeneous distribution of O, Ti and Ni also indicates the uniform dispersion of NiO on the surface of TiO_2 support. As TiO_2 and NiO are typical n-type and p-type semiconductors, respectively, the

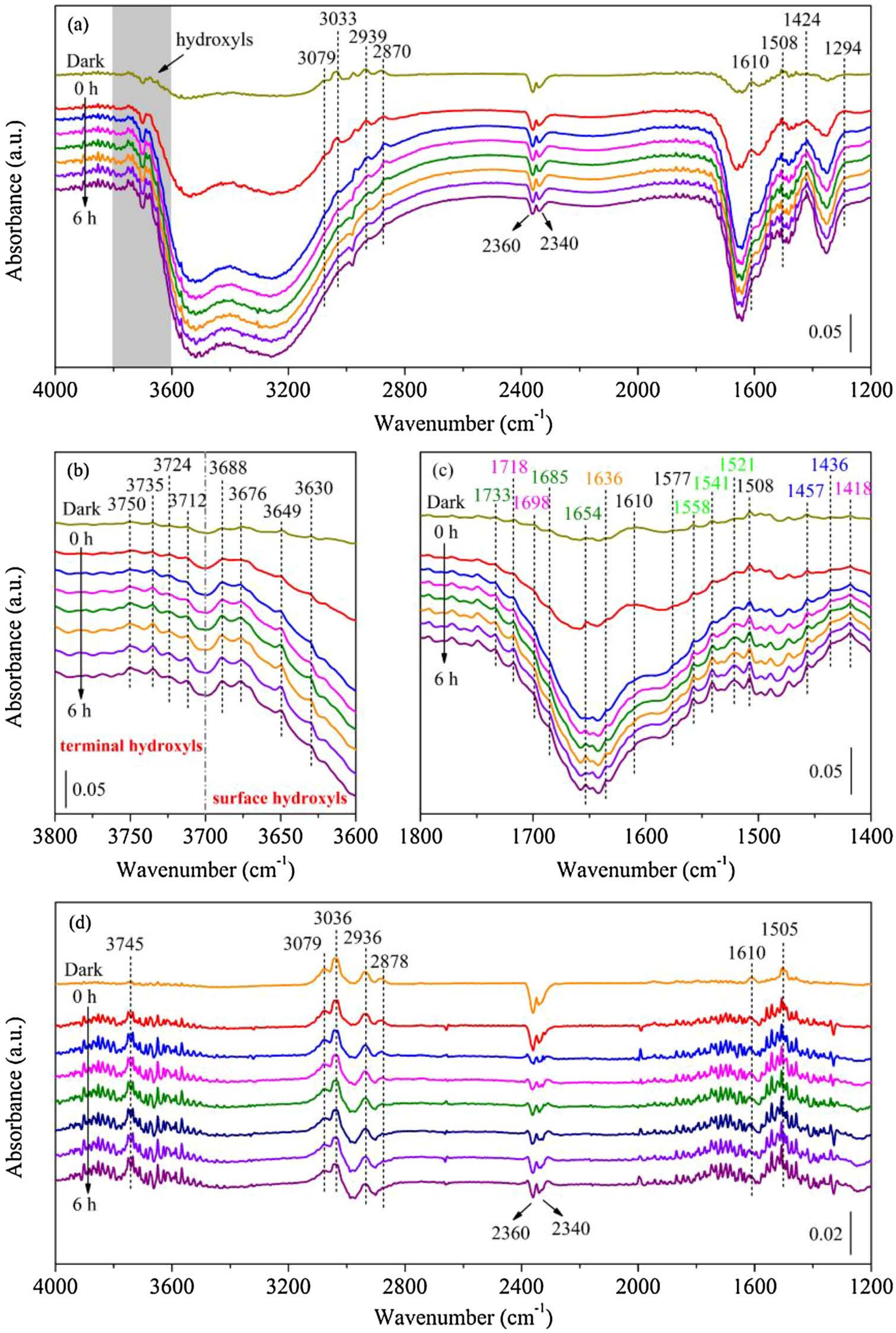

Fig. 8. (a) *In situ* FTIR spectra of toluene photo-oxidation on the NiO/TiO_2(1–6) composite collected at different illumination times under Xe-lamp irradiation, (b) and (c) enlarged FTIR spectra at the wavenumber range of 3800-3600 and 1800–1400 cm^{-1} from Fig. 8a, and (d) *in situ* FTIR spectra of toluene photo-oxidation on TiO_2 NRs.

interfacial connection in *p-n* junctions could serve as migration paths to facilitate the charge separation and induce synergistic effects to accelerate the photocatalytic reactions.

3.2.2. XPS analysis

XPS analysis was performed to investigate the atomic environment of the catalysts. Fig. 4a compares the XPS spectra of Ti 2p from TiO_2 NRs and NiO/TiO_2(1/6). The characteristic doublets of Ti^{4+} centered at 464.1 and 458.4 eV are assigned to Ti $2p_{1/2}$ and Ti $2p_{3/2}$, respectively [33,34]. For NiO/TiO_2(1/6) sample, the chemical state or coordinated environment is considered to be changed by the coupling of NiO with TiO_2 NRs, as the location of the characteristic doublets of Ti^{4+} slightly shifts to a higher binding energy by ~0.2 eV. Fig. 4b displays the XPS spectra of O 1 s of various catalysts, which are fitted into two sub-bands. The band centered at 531.7 eV (O_α) is assigned to the surface adsorbed oxygen species (oxygen vacancy, hydroxyl-like group or the chemisorbed water), and the peak at 529.5 eV (O_β) is deemed as the lattice oxygen species [35–37]. More hydroxyl-like group may exist on TiO_2 NRs, which could be derived from the remained $H_2Ti_3O_7$ phase in TiO_2 NRs. The O 1 s XPS spectrum of black NiO is displayed in Fig. S3 (Supporting Information), which exhibits the similar oxygen species in O_α and O_β to the TiO_2 NRs and NiO/TiO_2(1/6), and the blue shift of the characteristic peaks could be due to the possible lattice defects in the black NiO.

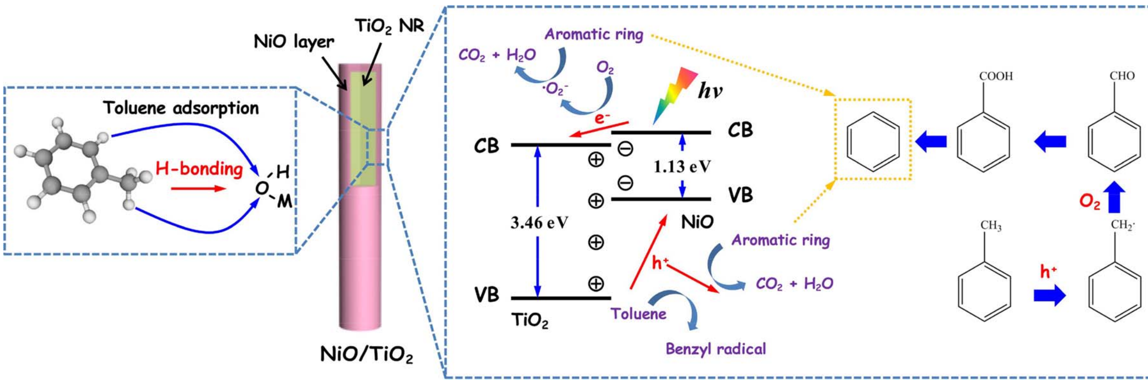

Fig. 9. Proposed mechanism for the enhanced activity of NiO/TiO_2 heterojunctions in the photo-oxidation of toluene.

Fig. 4c displays the XPS spectra of Ni 2p of NiO and NiO/TiO_2(1/6) samples. The main Ni $2p_{3/2}$ peak is located around 853.6 eV along with two satellite bands: one at ~1.8 eV higher BE (sat I) and the other at ~7.7 eV higher BE (sat II), and the Ni $2p_{1/2}$ is located at ~872.8 eV with a satellite band at 879.9 eV. The main Ni $2p_{3/2}$ peak (853.6 eV) and sat II (861.3 eV) are attributed to Ni^{2+}, while the origin of sat I (855.4 eV) is still unclear. Except for the ascription to the species related to some surface defects, such as Ni^{3+}, Ni^{2+}-OH and Ni^{2+} vacancies [38–41], the peak also reflects the dispersion of NiO on the support. Recent cluster model calculations indicate that the satellite at the higher binding energy of ~1.5 eV from the main line of Ni $2p_{3/2}$ can be ascribed to the surface NiO_5 species with a pyramidal symmetry, while the main signal is due to the bulk NiO_6 (octahedra) [14]. The intensity ratio of sat I to the main line of Ni $2p_{3/2}$ has been calculated, interpreting that the ratio on NiO/TiO_2(1/6) is increased to 2.11 from 0.77 on the pure NiO. Although the attribution of sat (I) is still in debate, an elevated signal of sat (I) accompanied with a weakened intensity of the main line is considered to benefit the photocatalytic performance of NiO/TiO_2 by generating more surface defects or improving the dispersion of NiO on TiO_2 NRs. The introduced surface defects may provide additional energy levels to narrow the band gap, and the better dispersion of NiO means a stronger interaction between the NiO and TiO_2 support, which facilitates the formation of heterojunctions between NiO and TiO_2 to improve the charge separation. The tight bound between NiO and TiO_2 species could be further confirmed by the location shift of the characteristic doublets of Ti^{4+} as discussed before.

3.2.3. Structure of energy band

DRS of various samples and the corresponding band gap energies estimated from the Tauc's plots by $(\alpha h\nu) = A(h\nu\text{-}E_g)^{1/2}$ are shown in Fig. 5a and b, respectively, to reflect the sunlight response and absorption ability of TiO_2 NRs, black NiO and NiO/TiO_2 hybrids [42]. From Fig. 5a, the light absorption of TiO_2 NRs rises rapidly at the beginning of ~380 nm, and the corresponding band gap is 3.46 eV. The black NiO exhibits a high response to the visible light, with a band gap of 1.42 eV. Due to the coupling of TiO_2 with the as-prepared black NiO with a narrow band gap, all the NiO/TiO_2 samples with various TiO_2/NiO ratios exhibit the enhanced light absorption and decreased band gaps, which greatly favor the photocatalytic reaction.

Then Mott-Schottky (M-S) plots and VB-XPS curves were measured on TiO_2 NRs, black NiO and NiO/TiO_2(1/6) samples. From Fig. 5c, the M-S plots for electrodes made of TiO_2 NRs, black NiO and NiO/TiO_2(1/6) indicate the flat band potentials at −0.09, 0.56 and −0.49 V *vs* NHE in the dark, respectively, obtained from the *x* intercept of the linear region. The distances from VB edge levels of photocatalysts to the Fermi level (E_f) can be obtained by VB-XPS (Fig. 5d), which are 2.93, 0.49 and 0.26 eV for TiO_2 NRs, black NiO and NiO/TiO_2(1/6) samples, respectively.

The flat band potential reflects the differences between the Fermi levels and water-reduction potential of various samples [43]. Herein, the approximate valence band (VB) edge level can be inferred from the M–S plots and VB-XPS. The position of conduction band (CB) is obtained by the equation of $E_{CB} = E_{VB} - E_g$, in which E_g represents the band gap of a semiconductor obtained by DRS. The band structures of the three catalysts are presented in Fig. 6. From Fig. 5c, TiO_2 NRs and black NiO are typical *n*-type and *p*-type semiconductors, respectively, thus the Fermi levels of the TiO_2 NRs and NiO are close to the CB of TiO_2 and the VB of NiO, respectively. When *n*-type TiO_2 NRs are composited with *p*-type NiO, *p-n* heterojunctions between the two materials are formed, resulting in the realignment of their valence and conduction bands due to the thermal equilibrium of the different Fermi levels and generation of the built-in electric field. Attributed to the formation of the built-in electric field and the realignment of VB and CB of TiO_2 NRs and NiO, the recombination of the photo-generated electrons and holes is greatly inhibited, benefiting the more effective charge separation and more rapid charge transfer to the catalyst [21,44]. The improved charge separation and transfer are proved by the photoelectric measurements, as presented in Fig. S4 in the Supporting Information. From Fig. S4, the NiO/TiO_2(1/6) exhibits the enhanced photocurrent compared with TiO_2, as well as the increased stability, illustrating the more effective separation of photogenerated electron-hole pairs [32]. It is well know that the semicircle diameter of the EIS plot is equal to the charge transfer resistance, herein the depressed semicircles of NiO/TiO_2(1/6) at high frequencies interprets the decreased resistance of charge transfer and faster interfacial charge transfer [45].

3.3. Reaction pathway of photo-oxidation of toluene

In situ FTIR is an efficient technology to monitor the transient species and states adsorbed on catalyst surface. Fig. 7 displays *in situ* FTIR spectra of TiO_2 NRs and NiO/TiO_2(1/6) samples during the adsorption of toluene in dark on a real-time, as well as the spectra after toluene saturation (90 min). The bands in the range of 3200-2800 and 1600–1250 cm^{-1} are attributed to the features of toluene, which has been analyzed below. The band at 3800–3600 cm^{-1} on NiO/TiO_2(1/6) is ascribed to the ν(M-OH) vibration mode (M represents Ti or Ni), and the broad band centered at ~3400 cm^{-1} is assigned to the vibration band of H-bonding [46,47]. It is observed that, with the increasing adsorption time, the signal intensity of M-OH is gradually decreasing, accompanied with the elevated signal of H-bonding, suggesting the strong adsorption of toluene accomplished by the interaction of the methyl or aromatic ring with the catalyst surface, whereas the changes of Ti-OH and H-bonding bands are not obvious on TiO_2 NRs. Herein, the enhanced adsorption of toluene on NiO/TiO_2(1/6) is speculated to be enforced by the generation of H-bonding. From a previous study, the H-bonding could also be caused by the changed adsorption energy of

toluene on the catalyst surface after the deposition of NiO [48]. Besides the facilitated adsorption of toluene, H-bonding was also reported to play a crucial role in the stabilization of surface-trapped holes in the photocatalytic water splitting reaction [49]. Similarly, the H-bonding with adsorbed toluene may also benefit to elevating the mobility of holes and suppressing the recombination of photo-generated charge carriers on $NiO/TiO_2(1/6)$.

Fig. 8 presents *in situ* FTIR spectra of the photo-oxidation of toluene on $NiO/TiO_2(1/6)$ and TiO_2 samples. After the adsorption equilibrium of toluene on $NiO/TiO_2(1/6)$, the characteristic vibrations of toluene are detected, where the bands centered at 3079 and 3033 cm^{-1} are assigned to the C–H stretching mode of the aromatic ring, the bands around 2939 and 2870 cm^{-1} are attributed to the C–H stretching vibration of methyl, and the bands at 2360 and 2340 cm^{-1} correspond to CO_2 (Fig. 8a). The feature bands of hydroxyl groups are located at the range of 3800–3600 cm^{-1} and act as the main adsorption sites for toluene, including the bridged –OH (3688, 3676, 3649 and 3630 cm^{-1}) and terminal hydroxyls (3750, 3735, 3724 and 3712 cm^{-1}), as shown in Fig. 8b [29,46,49]. In the low wavenumber range (Fig. 8a and c), the bands at 1610, 1577 and 1508 cm^{-1} are assigned to the skeleton stretching vibrations of the aromatic ring, the bands at 1457 and 1436 cm^{-1} are caused by the asymmetric methyl bending vibration, and the band at 1636 cm^{-1} is assigned to the bending mode of physisorbed water [50,51]. During the irradiation, the intensity of toluene bands decreases gradually, and at the same time, some new IR bands appear. The bands at 1733 and 1685 cm^{-1} are reported as the ν(C=O) mode of an aldehyde group and the vibrational mode of a carbonyl group, respectively, along with the bands around 1654 and 1577 cm^{-1} for the ν(C=C) skeleton vibrations of the aromatic ring, illustrating the formation of benzaldehyde. The bands around 1558, 1541, and 1521 cm^{-1} are attributed to the asymmetric stretching vibration of the carboxylate group COO^-, implying the presence of benzoic acid [52,53]. According to the reaction pathway proposed by Sleiman and Zhan [54,55], benzaldehyde and benzene are the main intermediates in the photo-oxidation of toluene, which are further oxidized after opening reactions of the aromatic ring. The presence of oxalic acid with the bands at 1718, 1698 and 1418 cm^{-1} for the ν(C=O), ν(C–O) and ν(C–C) of oxalic acid proves the opening of the aromatic ring [56].

Fig. 8d displays the *in situ* FTIR spectra of the photo-oxidation of toluene on TiO_2, and the stable features of toluene (3079, 3036, 2936, 1610 and 1505 cm^{-1}) during the irradiation interpret the poor activity of TiO_2 NRs. The activation of toluene to the intermediates of benzaldehyde, benzoic acid or oxalic acid could not be clearly shown at the range of 2000–1400 cm^{-1}, and is confirmed by the stable peaks of aromatic ring centered at 1610 and 1505 cm^{-1}. The *in situ* FTIR spectra for the photo-oxidation of toluene on $NiO/TiO_2(1/10)$ and $NiO/TiO_2(1/2)$ samples were also investigated (Fig. S6). From Fig. 8 and Fig. S6, the intensities of the bands at 1610 and 1508 cm^{-1} on $NiO/TiO_2(1/10)$ sample after irradiation for 6 h, which are attributed to the skeleton stretching vibrations of the aromatic ring, are much higher than those on $NiO/TiO_2(1/6)$ and $NiO/TiO_2(1/2)$ samples. Herein, the introduced NiO with higher loading is speculated to facilitate the opening of aromatic ring, which could also be proved by the similar performance of $NiO/TiO_2(1/6)$ and $NiO/TiO_2(1/10)$ samples (Fig. 1). For the slightly enhanced activity of $NiO/TiO_2(1/6)$ compared with $NiO/TiO_2(1/2)$, it may be attributed to the better dispersion of NiO on the surface of TiO_2 NRs due to the most appropriate loading.

According to previous reports [52,57], toluene is attacked by photo-generated h^+ at low humidity, leading to the production of a benzyl radical, and the subsequent reaction of aromatic ring opening is dependent on the attacking of h^+ or $\cdot O_2^-$. The introduction of NiO is beneficial for increasing the mobility of h^+ in NiO/TiO_2 hybrids, and the generation of $\cdot O_2^-$ under irradiation is confirmed by the ESR measurement (Fig. S6, Supporting Information). However, $\cdot$OH is not observed on NiO/TiO_2 and pristine TiO_2 NRs. These results suggest effective separation of the photo-generated charges and long-lived photo-induced electron-holes in NiO/TiO_2 [29,58].

From the physicochemical properties, band structure, and the *in situ* FTIR spectra of the surface adsorbed intermediates on $NiO/TiO_2(1/6)$ during the adsorption-oxidation of toluene, a possible mechanism for the enhanced photocatalytic activity of NiO/TiO_2 heterojunctions is proposed (Fig. 9). When a black NiO nanocluster was formed on the surface of TiO_2 NRs, a *p-n* heterojunction is constructed by the *p*-type NiO and *n*-type TiO_2, which greatly enhances the separation of photo-generated electron-hole pairs and efficiently suppresses the recombination by the built-in field. For the adsorption-oxidation of toluene, the NiO/TiO_2 hybrid exhibits a more efficient adsorption for toluene induced by the formation of H-bonding. Moreover, the occupation of surface hydroxyls due to toluene adsorption results in the reservation of h^+ to participate in the formation of the benzyl radical to induce reactions of aromatic ring opening. Under irradiation, the narrow band gap of black NiO causes more excited electrons in the conduction band of NiO, which transfer to the conduction band of TiO_2 and react with the oxygen to form $\cdot O_2^-$. The produced $\cdot O_2^-$ as well as h^+ act as the primary species to open the aromatic ring to generate benzyl radical for oxidation, following benzyl radical → benzaldehyde → benzoic acids → benzene, and finally to CO_2 and H_2O.

Overall, compared with the traditional TiO_2 material, the introduction of black NiO makes the as-prepared $NiO/TiO_2(1/6)$ catalyst a greatly enhanced light response, and the generated *p-n* heterojunctions favor the inhibition of the combination of photo-generated electrons and holes. Moreover, the coupling of NiO and TiO_2 also enhances the adsorption of toluene on the catalyst surface by the generation of H-bonding, which consumes the surface hydroxyls and improves the mobility of holes, and thus enhances the generation of $\cdot O_2^-$ to participate the oxidation of toluene.

4. Conclusions

A *p*-type black NiO is successfully coupled to the surface of *n*-type TiO_2 NRs by a facile hydrothermal method. The quite narrowed band gap of black NiO (E_g = 1.42 eV), resulting from its lattice defects and nanoscale size, causes much stronger sunlight response, and the *p-n* heterojunction between NiO and TiO_2 NRs benefits the separation of photo-generated electrons and holes and suppression of their recombination on the catalyst surface. The photocatalytic activity of the as-prepared heterojunction at an appreciate ratio of NiO/TiO_2 (molar ratio of 1/6) is enhanced significantly, achieving a photocatalytic rate of 7.94 times of that on the pristine TiO_2 NRs in photo-oxidation of gas-phase toluene. *In situ* FTIR measurements revealed that the surface hydroxyl groups on NiO/TiO_2 (1/6) provide the efficient sites for toluene adsorption by forming H-bonding, and that the generated $\cdot O_2^-$ and h^+ with a longer life contribute to the rapid opening of aromatic ring for oxidative degradation.

Acknowledgements

This work was supported financially by the National Natural Science Foundation of China (21507029, 21501138), Natural Science Foundation of Hebei Province (B2016502063), Open Foundation of Key Laboratory of Industrial Ecology and Environmental Engineering (KLIEEE-15-02), and China Ministry of Education and the Fundamental Research Funds for the Central Universities (2016MS109).

Appendix A. Supplementary data

Supplementary data associated with this article can be found, in the online version, at http://dx.doi.org/10.1016/j.apcatb.2017.11.028.

References

[1] K. Zhang, W. Zhou, X. Zhang, B. Sun, L. Wang, K. Pan, B. Jiang, G. Tian, H. Fu, Appl.

Catal. B: Environ. 206 (2017) 336–343.
[2] J. Liu, J. Ke, D. Li, H. Sun, P. Liang, X. Duan, W. Tian, M.O. Tade, S. Liu, S. Wang, ACS Appl. Mater. Interfaces 9 (2017) 11678–11688.
[3] J. Ke, X. Duan, S. Luo, H. Zhang, H. Sun, J. Liu, M. Tade, S. Wang, J. Chem. Eng. 313 (2017) 1447–1453.
[4] Z. Liu, H. Li, K. Liu, H. Yu, K. Cheng, Sol. Energy 142 (2017) 61–67.
[5] B. Liu, X. Li, Q. Zhao, Y. Hou, G. Chen, J. Mater. Chem. A 5 (2017) 8909–8915.
[6] J. Wang, Y. Xia, H. Zhao, G. Wang, L. Xiang, J. Xu, S. Komarneni, Appl. Catal. B: Environ. 206 (2017) 406–416.
[7] J. Low, J. Yu, M. Jaroniec, S. Wageh, A.A. Al-Ghamdi, Adv. Mater. 29 (2017) 1601694–1601713.
[8] G. Zhu, J. Xu, W. Zhao, F. Huang, ACS Appl. Mater. Interfaces 8 (2016) 31716–31721.
[9] X. Liu, G. Zhu, X. Wang, X. Yuan, T. Lin, F. Huang, Adv. Energy Mater. 6 (2016) 1600452–1600480.
[10] K. Zhang, J.H. Park, J. Phys. Chem. Lett. 8 (2017) 199–207.
[11] J. Ke, X. Li, Q. Zhao, B. Liu, S. Liu, S. Wang, J. Colloid Interface Sci. 496 (2017) 425–433.
[12] Z. Liu, W. Xu, C. Qian, X. Chen, G. Jin, Renew. Energy 84 (2015) 89–96.
[13] J. Benjamin, A. Nail, J. Zhao, J. Wang, M. Greaney, R. Brutchey, F. Osterloh, ACS Nano 9 (2015) 5135–5142.
[14] Q. Jin, T. Ikeda, M. Fujishima, H. Tada, Chem. Commun. 47 (2011) 8814–8816.
[15] J. Liu, Y. Li, J. Ke, Z. Wang, H. Xiao, Catalysts 7 (2017) 30.
[16] C. Luo, D. Li, W. Wu, C. Yu, W. Li, C. Pan, Appl. Catal. B: Environ. 166–167 (2015) 217–223.
[17] J. Wang, S. Mao, Z. Liu, Z. Wei, H. Wang, Y. Chen, Y. Wang, ACS Appl. Mater. Interfaces 9 (2017) 7139–7147.
[18] Z. Zhang, C. Shao, X. Li, C. Wang, M. Zhang, Y. Liu, ACS Appl. Mater. Interfaces 2 (2010) 2915–2923.
[19] M. Wang, J. Han, Y. Hu, R. Guo, Y. Yin, ACS Appl. Mater. Interfaces 8 (2016) 29511–29521.
[20] S. Phivilay, A. Puretzky, K. Domen, I. Wachs, ACS Catal. 3 (2013) 2920–2929.
[21] J. Ke, J. Liu, H. Sun, H. Zhang, X. Duan, P. Liang, X. Li, M.O. Tade, S. Liu, S. Wang, Appl. Catal. B: Environ. 200 (2017) 47–55.
[22] J. Lin, J. Shen, R. Wang, J. Cui, W. Zhou, P. Hu, D. Liu, H. Liu, J. Wang, R.I. Boughton, Y. Yue, J. Mater. Chem. 21 (2011) 5106–5113.
[23] R. Gonçalves, H. Wender, P. Migowski, A. Feil, D. Eberhardt, J. Boita, S. Khan, G. Machado, J. Dupont, S. Teixeira, J. Phys. Chem. C 121 (2017) 5855–5863.
[24] L. Hou, S. Li, Y. Lin, D. Wang, T. Xie, J. Colloid Interface Sci. 464 (2016) 96–102.
[25] W. Zhou, W. Li, J. Wang, Y. Qu, Y. Yang, Y. Xie, K. Zhang, L. Wang, H. Fu, D. Zhao, J. Am. Chem. Soc. 136 (2014) 9280–9283.
[26] X. Chen, L. Liu, P. Yu, S. Mao, Science 331 (2011) 746–750.
[27] M. Ye, J. Jia, Z. Wu, C. Qian, R. Chen, P. O'Brien, W. Sun, Y. Dong, G. Ozin, Adv. Energy Mater. 7 (2017) 1601811–1601817.
[28] C. Bianchi, S. Gatto, C. Pirola, A. Naldoni, A. Michele, G. Cerrato, V. Crocellà, V. Capucci, Appl. Catal. B: Environ. 146 (2014) 123–130.
[29] J. Sun, X. Li, Q. Zhao, M. Tade, S. Liu, J. Mater. Chem. A 3 (2015) 21655–21663.
[30] F. Zhang, M. Wang, X. Zhu, B. Hong, W. Wang, Z. Qi, W. Xie, J. Ding, J. Bao, S. Sun, C. Gao, Appl. Catal. B: Environ. 170–171 (2015) 215–224.
[31] M. Zhou, J. Yu, S. Liu, P. Zhai, B. Huang, Appl. Catal. B: Environ. 89 (2009) 160–166.
[32] S. Luo, J. Ke, M. Yuan, Q. Zhang, P. Xie, L. Deng, S. Wang, Appl. Catal. B: Environ. 221 (2018) 215–222.
[33] Y. Zhang, C. Wang, H. Hou, G. Zou, X. Ji, Adv. Energy Mater. 7 (2017) 1600173–1600184.
[34] B. Ma, P. Guan, Q. Li, M. Zhang, S. Zang, ACS Appl. Mater. Interfaces 8 (2016) 26794–26800.
[35] J. Liu, X. Li, Q. Zhao, J. Ke, H. Xiao, X. Lv, S. Liu, M. Tadé, S. Wang, Appl. Catal. B: Environ. 200 (2017) 297–308.
[36] H. Li, W. Shi, W. Huang, E.P. Yao, J. Han, Z. Chen, S. Liu, Y. Shen, M. Wang, Y. Yang, Nano Lett. 17 (2017) 2328–2335.
[37] J. Liu, X. Li, R. Li, Q. Zhao, J. Ke, H. Xiao, L. Wang, S. Liu, M. Tadé, S. Wang, Appl. Catal. A: Gen. 549 (2018) 289–301.
[38] B. Solsona, J. López Nieto, P. Concepción, A. Dejoz, F. Ivars, M. Vázquez, J. Catal. 280 (2011) 28–39.
[39] H. Zhu, D. Rosenfeld, D. Anjum, S. Sangaru, Y. Saih, S. Ould-Chikh, J. Basset, J. Catal. 329 (2015) 291–306.
[40] Q. Liu, Z. Zhong, F. Gu, X. Wang, X. Lu, H. Li, G. Xu, F. Su, J. Catal. 337 (2016) 221–232.
[41] M. Sun, T. Bürgi, R. Cattaneo, D. van Langeveld, R. Prins, J. Catal. 201 (2001) 258–269.
[42] M. Tahir, N. Amin, J. Chem. Eng. 285 (2016) 635–649.
[43] L. Liao, Q. Zhang, Z. Su, Z. Zhao, Y. Wang, Y. Li, X. Lu, D. Wei, G. Feng, Q. Yu, X. Cai, J. Zhao, Z. Ren, H. Fang, F. Robles-Hernandez, S. Baldelli, J. Bao, Nature Nanotech. 9 (2014) 69–73.
[44] H. Wang, L. Zhang, Z. Chen, J. Hu, S. Li, Z. Wang, J. Liu, X. Wang, Chem. Soc. Rev. 43 (2014) 5234–5244.
[45] Z. Zhang, R. Dua, L. Zhang, H. Zhu, H. Zhang, P. Wang, ACS Nano 7 (2013) 1709–1717.
[46] M. El-Roz, M. Kus, P. Cool, F. Thibault-Starzyk, J. Phys. Chem. C 116 (2012) 13252–13263.
[47] Z. Liu, H. Li, G. Cao, Int. J. Env. Res. Pub. He. 14 (2017).
[48] L. Ren, Y. Li, J. Hou, J. Bai, M. Mao, M. Zeng, X. Zhao, N. Li, Appl. Catal. B: Environ. 181 (2016) 625–634.
[49] A. Litke, Y. Su, I. Tranca, T. Weber, E. Hensen, J. Hofmann, J. Phys. Chem. C Nanomater. Interfaces 121 (2017) 7514–7524.
[50] J. Liu, Y. Luan, C. An, J. Zhang, D. Wang, Y. Li, ChemCatChem 7 (2015) 2918–2923.
[51] B. Liu, X. Li, Q. Zhao, J. Ke, J. Liu, S. Liu, M. Tade, J. Colloid Interface Sci. 438 (2015) 1–6.
[52] A. Mamaghani, F. Haghighat, C. Lee, Appl. Catal. B: Environ. 203 (2017) 247–269.
[53] M. Hernández-Alonso, I. Tejedor, J. Coronado, M. Anderson, Appl. Catal. B: Environ. 101 (2011) 283–293.
[54] M. Sleiman, P. Conchon, C. Ferronato, J. Chovelon, Appl. Catal. B: Environ. 86 (2009) 159–165.
[55] S. Zhan, Y. Yang, X. Gao, H. Yu, S. Yang, D. Zhu, Y. Li, Catal. Today 225 (2014) 10–17.
[56] Y. Irokawa, T. Morikawa, K. Aoki, S. Kosaka, T. Ohwaki, Y. Taga, Phys. Chem. Chem. Phys. 8 (2006) 1116–1121.
[57] X. Qian, D. Yue, Z. Tian, M. Reng, Y. Zhu, M. Kan, T. Zhang, Y. Zhao, Appl. Catal. B: Environ. 193 (2016) 16–21.
[58] F. Dong, Q. Li, Y. Sun, W. Ho, ACS Catal. 4 (2014) 4341–4350.